Research on Fiber Bragg Grating Sensor Group for Three Dimensional In-situ Stress Measurement

Yimin Liu[1,2,4], Zhengyang Hou[3], Hao Zhou[2], Lu Yang[1,4], and Peng Wang[1,4]

[1] Tianjin Key Laboratory for Advanced Mechatronic System Design and Intelligent Control, School of Mechanical Engineering, Tianjin, 300384, China.
[2] National Institute of Natural Hazards, MEMC, Beijing,100085, China.
[3] State Key Laboratory of Remote Sensing Science, Faculty of Geographical Science, Beijing Normal University, Beijing, 100875, China.
[4] National Demonstration Center for Experimental Mechanical and Electrical Engineering Education (Tianjin University of Technology), Tianjin 300384, China.

Correspondence to: Zhengyang Hou (hou116106@163.com)

Abstract. The observation and estimation of deep crustal stress state is a key and difficult problem in in-situ stress measurement. The borehole wall strain gauge based on the overcoring stress relieving method is one of the main methods of in-situ stress measurement. In this paper, a strain sensing array based on FBG is designed by using the main structure of the classical hollow inclusion cell, and its layout scheme on the hollow inclusion is studied. According to the layout scheme, the in-situ stress inversion algorithm of hole-wall strain to stress is deduced; then, the triaxial loading and unloading experiment platform is built, and the calibration experiment of FBG strain sensor is designed; Finally, Abaqus finite element software is used to simulate the in-situ stress measurement process of the overcoring stress relieving. The FBG strain values of each measurement direction before and after the overcoring process are extracted, and the stress inversion equation is used to carry out the stress inversion. The comparison of the inversion results proved that the FBG strain sensor group is feasible and reliable. The quasi-distributed FBG sensor module designed in this paper can invert the three-dimensional in-situ stress by measuring the hole-wall strain, which lays a theoretical and experimental foundation for the development and application of FBG hole-wall strain gauge. It fairly makes up for the deficiency of the existing hole-wall strain gauge based on resistance strain gauge, provides direct and accurate observation way for hole-wall strain measurement, and has important practical value for the development of in-situ stress measurement technology.

1 Introduction

The undisturbed stress in rock mass is called geo-stress or in-situ stress (Amadei and Stephenson, 1997). Accurate determination of in-situ stress state of deep rock mass is one of the necessary ways to solve the difficult problems in the study of Rock mechanics of deep mining and Crustal Dynamics, so it is necessary to develop in-situ stress testing methods and techniques (Wang, 2014). Among the recommended methods for rock mass stress measurement and estimation published by ISRM (International Society for Rock Mechanics) in 2003 (Ulusay, 2014), the hydraulic fracturing method and

the overcoring stress relieving method are mainly recommended (Hill et al., 1993; Amadei and stephasson, 1997). The overcoring stress relieving method is an in-situ stress measurement method based on borehole, which inverses the in-situ stress field by detecting the strain and deformation in the process of releasing the core from the parent rock.

35 As early as 1951, Swedish scholar N.Hast began to use piezomagnetic (inductive) sensors to measure stress changes in the mining industry (hast, 1958). The hole-wall strain measuring instruments in the world are mainly CSIR triaxial hole-wall strain gauge (Leeman, 1971), (CSIRO)HI hollow inclusion cell (worotnicki and Walton, 1979) and Borre triaxial hole-wall strain gauge of Swedish National Electricity Authority(Sjöberg and Klasson, 2003), etc. Some scholars use (CSIRO)HI digital hollow inclusion cell to evaluate stress state in the rock mass near the coring point (iabichino, 2014). In China, there

40 are mainly CKX01 hellow inclusion triaxial strain gauge developed by Yangtze River academy of Sciences (Zhong et al., 2002), improved hollow inclusion cell with complete temperature compensation developed by University of Science and Technology Beijing (Cai et al., 2000) and KX2002 hollow inclusion triaxial strain cells developed by Institute of Geomechanics, Chinese Academy of Geological Sciences (Liu et al., 2011).

  As an improved hole-wall strain gauge, hollow inclusion cell uses multiple groups of resistance strain gauge with

45 temperature compensation as sensors to calculate the in-situ stress. The epoxy resin shell wrapped outside the resistance strain gauge is better bonded and coupled with the hole-wall. The photo of hollow inclusion cell and the layout diagram of strain gauges are shown in Figure 1. This gauge can measure the stress tensor in a single hole to obtain the three-dimensional stress state of rock mass, and form a set of standardized measurement procedures, which is one of the most applicable and reliable in-situ stress measurement methods(Cai et al., 2000; Liu et al., 2011; Yan et al., 2018).
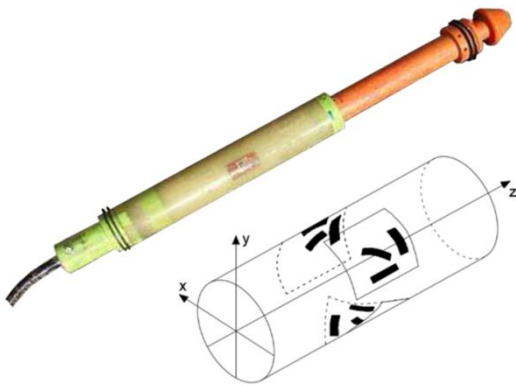
50

Figure 1: The photo of hollow inclusion cell and layout diagram of the strain gauges.

  At present, the h hollow inclusion cell is based on the traditional resistance strain gauge electrical testing instruments. They are generally vulnerable to the interference of temperature, vibration and other test environment factors, low measurement

55 success rate, less data, and other shortcomings, lack of more advanced in-situ stress measurement methods. FBG sensor has the advantages of small volume, high detection accuracy and spatial resolution, long sensing distance and strong anti

electromagnetic interference ability, so it is very suitable for the field of stress and strain detection in underground space, borehole wall, rock and soil mass (Hill and Meltz, 1997; Zhou et al., 2010). In recent years, researchers have done a lot of scientific research and engineering practice on FBG stress and strain sensors. American scholars fuhr et al. Buried 8 FBG strain sensors on the panel of Waterbury bridge on the winooski River in the United States, and detected the maximum strain value of 50 μ ε (Fuhr et al., 1998). Chinese academician Ou Jinping embeds the encapsulated FBG strain gauge into the reinforced concrete beam to measure the strain of concrete and steel bars inside it, and applies FBG technology to the field of health monitoring of major engineering structures (Ou, 2005). Zhang et al. compared the strain measurement by FBG with by resistance strain gauge, the results show that the linearity and sensitivity of the strain measurement data are in good agreement with the theoretical values, which proves that the method is effective and feasible (Zhang et al., 2001). Dewolf et al. design a vertical, unidirectional borehole strainmeter based on optical fiber to measure the earth strain (Dewolf et al., 2015). Zhong et al. designed FBG 3D geo-stress sensor, and conducted stress loading simulation experiment on the sensor device, and the monitoring results of the sensor are basically consistent with the actual load stress (Zhong et al., 2018). Maccioni et al. developed a three-axial fiber Bragg grating strain sensor for volcano monitoring, and the three-axial device showed a dynamic range of some hundreds of microstrains with microstrain resolution (submicrostrain concerning the vertical component) (Maccioni et al. 2019).

The above researches mainly focus on the health monitoring of engineering structures and the monitoring of dangerous rock mass and landslide. Up to now, the research and application of FBG strain detection technology in the field of in-situ stress measurement is less, there are only some borehole earth strainmeter, geo-stress sensor or volcano monitoring sensors based on optical fiber sensing technology, but there is less mature and stable in-situ measurement instrument and corresponding monitoring technology. In this paper, FBG sensing technology is used to develop hole-wall strain measurement technology in in-situ stress measurement, and a three-dimensional in-situ stress measurement sensor group based on FBG sensor array is designed. The arrangement of sensor array is mainly studied, and the in-situ stress inversion algorithm of FBG strain gauge is deduced, which lays an important theoretical and experimental foundation for the development and application of FBG hole-wall strain gauge.

2 The structural design

2.1 Main structure

Referring to the main structure of the resistance strain gauge hollow inclusion cell, the main structure and size are designed by using AutoCAD mechanical design software, and the hollow inclusion shell and deformation tube are manufactured by using 3D printing technology. Then the FBG strain sensor is encapsulated on the hollow inclusion shell and covered with an epoxy resin shell to couple with the hole-wall. The main structure is composed of two parts, which are hollow inclusion shell and piston guide. The tail of the piston guide is inserted into the hollow inclusion shell. The three-dimensional schematic diagram of the main structure is shown in Figure 2.
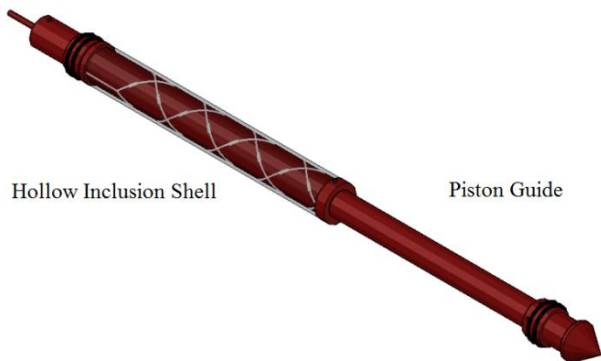
90   **Figure 2: The three-dimensional schematic diagram of the main structure.**

In Figure 3, the hollow inclusion shell in the main structure is composed of 1 ~ 11, and the piston guide is composed of 12 ~ 14. Before installation, the tail of the piston guide is inserted into the hollow inclusion shell, the glue capsule 10 in the hollow inclusion shell is filled with the prepared epoxy resin, and the piston and the shell are connected by an aluminum

95   wire through the pin hole 11. The main body of the guiding part of the piston is made of 3D printing, and the top is a conical guider 14. There is a hollow channel in the center of the piston, which is connected with the rubber outlet hole 13, and below the rubber outlet hole are two block circles 4.
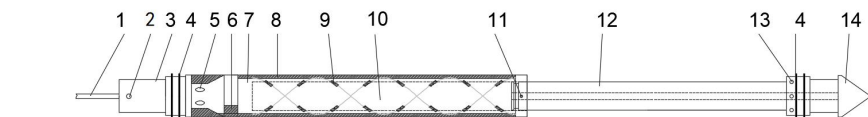
1 Sensing optical fiber 2 Locating pin 3 Mounting rod 4 block circle 5 threading hole 6 conductor groove 7 tube body 8 epoxy resin 9

100   FBG sensor group 10 Glue capsule 11 pin hole 12 piston rod 13 rubber outlet hole 14 conical guider

Figure 3: Schematic diagram of the main structure.

The hollow inclusion shell is the load-bearing matrix of FBG sensor, which adopts three-layer structure design, as shown in Figure 4. The inner layer is a hollow matrix, which is used to store epoxy resin binder; the second layer is a thin PVC

105   deformation tube which is sheathed on the hollow inclusion shell substrate, on which FBG sensor array is pasted. There is a gap between the deformation tube and the matrix, which can eliminate the interference of the matrix with higher hardness to the epoxy resin. The outermost layer is encapsulated with epoxy resin to protect the FBG sensor and play the role of strain coupling.
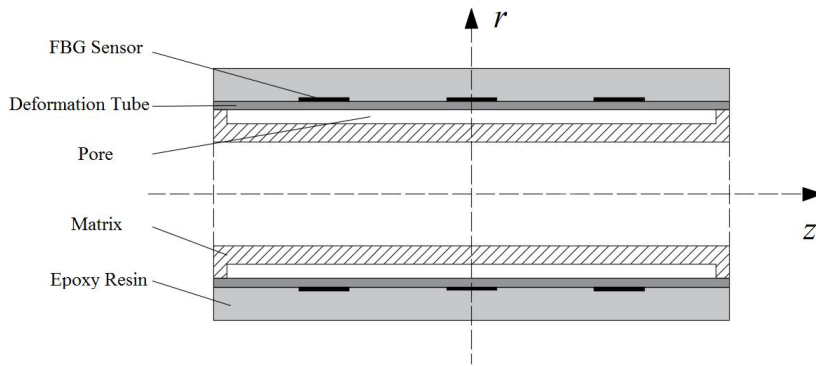
110 **Figure 4: Three-layer structure mode of hollow inclusion cell.**

2.2 Design and layout of FBG sensor group

The FBG strain sensor group adopts the installation mode of multi-group distributed winding, and twenty-six FBG sensing elements are arranged on the surface of the deformed tube by using six optical fibers. The layout position of the sensor group

115 is shown in Figure 5. The rectangle is the expanded deformed pipe wall surface, which is divided into two areas: A and B. the same color represents FBG sensor arranged on the same fiber.
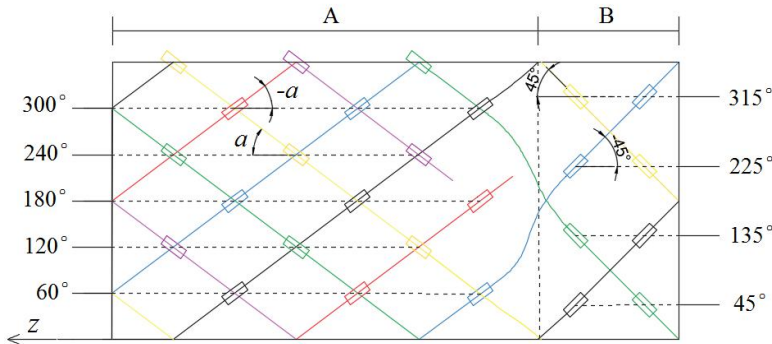
Figure 5: The layout position of the sensor group.

120 There are eighteen FBG sensors in area A, and the axial angle between the sensor and the tube is α (α = arctan 0.75), which are respectively arranged in the circumferential direction of 0°, 60°, 120°, 180°, 240° and 300° of the tube; there are eight FBG sensors in area B, and the axial angle between the sensor and the tube is ±45°, which are respectively arranged in the circumferential direction of 45°, 135°, 225° and 315° of the tube. The sensors in two areas A and B are distributed symmetrically. According to the principle of the same group of FBG with the same measurement direction and symmetrical

125 position, twenty-six sensors are divided into seven groups, corresponding to (A1 ~ B4) as shown in Figure 6.
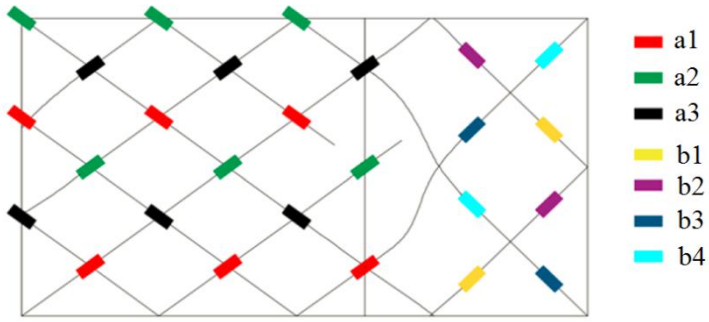
Figure 6: Schematic diagram of sensor equivalent measurement position.

The corresponding spatial orientation of each sensors group is shown in Table 1.

130 **Table 1: The corresponding spatial orientation of each sensors group.**

Group	Quantity	Position($\alpha=\arctan 0.75$)
a1	6	ε_α^{240}、$\varepsilon_{-\alpha}^{60}$
a2	6	ε_α^{0}、$\varepsilon_{-\alpha}^{180}$
a3	6	ε_α^{120}、$\varepsilon_{-\alpha}^{300}$
b1	2	ε_{45}^{45}、ε_{-45}^{225}
b2	2	ε_{45}^{135}、ε_{-45}^{315}
b3	2	ε_{45}^{225}、ε_{-45}^{45}
b4	2	ε_{45}^{315}、ε_{-45}^{135}

The strain vectors corresponding to different groups of strain sensors are not correlated with each other. According to the stress inversion calculation method of hole-wall strain method and the in-situ stress calculation principle of hollow inclusion cell (Leeman, 1964; Cai, 2000), any six strain measurement data from different groups can be used to calculate the three-135 dimensional stress tensor. The FBG sensor group designed in this paper has seven different spatial orientations, so the three-dimensional stress tensor can be solved theoretically.

3 In-situ stress inversion algorithm

The stress inversion of FBG strain sensor group can be approximately regarded as the stress and strain problems on and around the borehole surface under the action of three-dimensional stress field. According to the elastic theory, the stress inside the borehole can be calculated from the strain of hole-wall, and then the original rock stress state can be obtained (Cai, 2000). In the specific calculation, it involves the transformation of stress components in geodetic coordinate system O-*xyz*, drilling rectangular coordinate system O-*x′y′z′* and drilling cylindrical coordinate system O-*z′ρθ* (Hou, 2020). Firstly, the stress transformation relationship between the cylindrical coordinate system and the drilling rectangular coordinate system is established. According to Hooke's theorem and the azimuth angle of FBG sensor, the relationship equation between the FBG strain and the stress component in the drilling rectangular coordinate system is obtained. Then, through the coordinate transformation equation, the stress component in the geodetic coordinate system is used to represent the strain equation in the drilling coordinate system. To solve this equation, the least square solution is the stress component in the geodetic coordinate system. The diagram of the spatial relationship of the coordinate system is shown in the left figure of Figure 7.
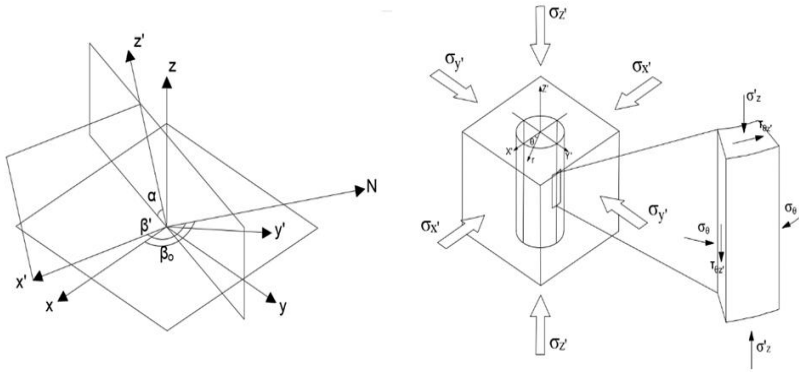
Figure 7: The diagram of the spatial relationship of the coordinate system.

3.1 Relation equation of the strain component of hole-wall

The micro element is taken at the position of the hole-wall, and the hole-wall can be regarded as a plane in a small scale, the stress state of the hole-wall in the plane is shown in the right figure of Figure 7. According to Hooke's law, the two-dimensional stress-strain relationship of the hole-wall under the drilling column coordinate system is as follows:

$$\varepsilon_\theta = \frac{1}{E}\left(\sigma_\theta - \nu\sigma_z'\right) \tag{1}$$

$$\varepsilon_z' = \frac{1}{E}\left(\sigma_z' - \nu\sigma_\theta\right) \tag{2}$$

$$\gamma_{\theta z'} = \frac{\left(\varepsilon_{z'} - \varepsilon_\theta\right) + \left(\varepsilon_{z'} - \varepsilon_\theta\right)\cos 2\varphi - 2\varepsilon_\varphi}{\sin 2\varphi} = \frac{\tau_{\theta z'}}{G} \tag{3}$$

Where, σ_θ represents the stress in the direction of θ axis, $\tau_{\theta z'}$ and $\gamma_{\theta z'}$ are the shear stress and shear strain on plane θ-z' respectively, ε_φ represents the hole-wall strain in the φ direction, E and G are elastic modulus and shear modulus of surrounding rock respectively, and ν is Poisson's ratio of surrounding rock. Let r = a (at the hole-wall), , the equations transformed the stress component at (r, θ, z') in borehole cylindrical coordinate system into the stress in the rectangular coordinate system is as follows:

$$\varepsilon_\theta = \frac{1}{E}\left\{\left(\sigma_{x'}+\sigma_{y'}\right)+2\left(1-\nu^2\right)\left[\left(\sigma_{y'}-\sigma_{x'}\right)\cos 2\theta - 2\tau_{x'y'}\sin 2\theta\right]-\nu\sigma_{z'}\right\} \tag{4}$$

$$\varepsilon_z' = \frac{1}{E}\left[\sigma_{z'} - \nu\left(\sigma_{x'}+\sigma_{y'}\right)\right] \tag{5}$$

$$\gamma_{\theta z} = \frac{4}{E}\left(1+\nu\right)\left(\tau_{y'z'}\cos\theta - \tau_{x'z'}\sin\theta\right) \tag{6}$$

Using the two-dimensional strain component of the hole-wall in the cylindrical coordinate system, the linear strain $\varepsilon_\varphi^\theta$ at any point and in any direction of the hole-wall can be expressed, where θ is the azimuth of the line strain measurement point.

$$\varepsilon_\varphi^\theta = \frac{1}{2}\left[\left(\varepsilon_z'+\varepsilon_\theta\right)+\left(\varepsilon_z'-\varepsilon_\theta\right)\cos 2\varphi - \gamma_{\theta z}\sin 2\varphi\right] \tag{7}$$

3.2 Stress inversion equation based on FBG arrangement

According to the layout scheme of FBG strain sensor group, the θ and φ values of seven equivalent orientations are brought into equation 7, and the relationship equation between the strain measurement value and each stress component in the drilling rectangular coordinate system is obtained as follows:

$$\vec{\varepsilon} = \frac{1}{E}N\cdot\vec{\sigma}' \tag{8}$$

Wherein, $\vec{\varepsilon}$ is the strain measurement value of a single sensor array, N is the stress-strain relation matrix, and $\vec{\sigma}$ is the stress component in geodetic coordinate system. According to the orientation of the sensor, there is $\vec{\varepsilon} = \left(\varepsilon_{-\alpha}^{60} \quad \varepsilon_{-\alpha}^{180} \quad \varepsilon_{-\alpha}^{300} \quad \varepsilon_{45}^{45} \quad \varepsilon_{45}^{135} \quad \varepsilon_{45}^{225} \quad \varepsilon_{45}^{315}\right)^T$. The stress-strain relationship matrix is as follows, and *K₁, K₂, K₃* and *K₄* are correction factors of the epoxy resin influence effect.

$$N = \begin{pmatrix} N_1-N_2 & N_1+N_2 & N_3 & N_4 & -N_5 & N_6 \\ N_1+2N_2 & N_1-2N_2 & N_3 & 0 & -2N_5 & 0 \\ N_1-N_2 & N_1+N_2 & N_3 & -N_4 & -N_5 & -N_6 \\ N_7 & N_7 & N_8 & N_9 & N_{10} & -N_{10} \\ N_7 & N_7 & N_8 & -N_9 & -N_{10} & -N_{10} \\ N_7 & N_7 & N_8 & N_9 & -N_{10} & N_{10} \\ N_7 & N_7 & N_8 & -N_9 & N_{10} & N_{10} \end{pmatrix} \tag{9}$$

Wherein, $N_1 = \dfrac{9}{25}K_1 - \dfrac{16}{25}v$, $N_2 = \dfrac{9}{25}K_2(v^2-1)$, $N_3 = \dfrac{16}{25} - \dfrac{9}{25}K_4 \cdot v$, $N_4 = \dfrac{18\sqrt{3}}{25}K_2(V^2-1)$, $N_5 = \dfrac{24}{25}K_3(1+v)$,

$N_6 = \dfrac{24\sqrt{3}}{25}K_3(1+v)$, $N_7 = \dfrac{1}{2}(K_1 - v)$, $N_8 = \dfrac{1}{2}(1-K_4 v)$, $N_9 = 2K_2(v^2-1)$ and $N_{10} = \sqrt{2}K_3(v+1)$ (Fama and Pender, 1980).

Since some FBG sensors are symmetrical in space, the formula 8 is also applicable to other FBG sensors in space, such as

185 $\vec{\varepsilon}' = \begin{pmatrix} \varepsilon_\alpha^{240} & \varepsilon_\alpha^0 & \varepsilon_\alpha^{120} & \varepsilon_{-45}^{225} & \varepsilon_{-45}^{315} & \varepsilon_{-45}^{45} & \varepsilon_{-45}^{135} \end{pmatrix}^T$. In order to obtain the three-dimensional stress state of rock mass in

the geodetic coordinate system, it is necessary to transform the stress component in the borehole coordinate system, the

transformation matrix is as follows:

$$\sigma_{i'j'} = \sum_{i=1}^{3}\sum_{i=1}^{3}\sigma_{ij}L_{ii'}L_{jj'} \tag{10}$$

In equation 10, $\sigma_{i'j'}$ is the stress component in the borehole coordinate system, $L_{ij'}$ is the cosine of each axis angle between the

190 borehole coordinate system and the geodetic coordinate system. Taking them into equation 8, the solution equation of each

rock stress component in geodetic coordinate system is obtained.

$$\vec{\varepsilon} = \frac{1}{E}N \cdot A \cdot \vec{\sigma} \tag{11}$$

The transformation matrix of coordinate is shown in equation 12.

$$A = \begin{pmatrix} L_{11'}^2 & L_{23'}^2 & L_{31'}^2 & 2L_{11'}L_{21'} & 2L_{21'}L_{31'} & 2L_{11'}L_{31'} \\ L_{12'}^2 & L_{22'}^2 & L_{32'}^2 & 2L_{12'}L_{22'} & 2L_{22'}L_{32'} & 2L_{12'}L_{32'} \\ L_{13'}^2 & L_{23'}^2 & L_{33'}^2 & 2L_{13'}L_{23'} & 2L_{23'}L_{33'} & 2L_{13'}L_{33'} \\ L_{11'}L_{12'} & L_{21'}L_{22'} & L_{31'}L_{32'} & L_{11'}L_{22'}+L_{12'}L_{21'} & L_{21'}L_{32'}+L_{31'}L_{22'} & L_{11'}L_{32'}+L_{31'}L_{12'} \\ L_{12'}L_{13'} & L_{22'}L_{23'} & L_{32'}L_{33'} & L_{12'}L_{23'}+L_{22'}L_{13'} & L_{22'}L_{32'}+L_{32'}L_{23'} & L_{12'}L_{33'}+L_{32'}L_{13'} \\ L_{11'}L_{13'} & L_{21'}L_{23'} & L_{31'}L_{33'} & L_{11'}L_{23'}+L_{21'}L_{13'} & L_{21'}L_{33'}+L_{31'}L_{23'} & L_{11'}L_{33'}+L_{31'}L_{13'} \end{pmatrix} \tag{12}$$

195 $L_{ij'}$ is shown in Table 2, where β_0, β', and α_0 are shown in Figure 9.

Table 2: Direction cosine of local coordinate system O-*x'y'z'* relative to global coordinate system O-*xyz*.

Coordinate	x	y	z
x'	$L_{11'} = \cos(\beta_0 - \beta')$	$L_{21'} = \sin(\beta_0 - \beta')$	$L_{31'} = 0$
y'	$L_{12'} = \sin\alpha_0 \sin(\beta_0 - \beta')$	$L_{22'} = \sin\alpha_0 \cos(\beta_0 - \beta')$	$L_{32'} = \cos\alpha_0$
z'	$L_{13'} = \cos\alpha_0 \sin(\beta_0 - \beta')$	$L_{23'} = -\cos\alpha_0 \cos(\beta_0 - \beta')$	$L_{33'} = \sin\alpha_0$

Take the equation $\Delta\lambda_B = \lambda_B(1-P_\alpha)\varepsilon$, between the wavelength variation of FBG and the measured strain into equation 11,

the stress inversion equations are obtained as follows:

$$\vec{k}_\lambda = \frac{1-P_\alpha}{E} N \bullet A \bullet \vec{\sigma} \qquad (13)$$

$$k_\lambda = \frac{\lambda_\varepsilon - \lambda_B}{\lambda_B} \qquad (14)$$

Among them, $\vec{k}_\lambda$ is the vector composed of wavelength shift ratio of FBG at each position, λ_ε is the wavelength value under strain state, and λ_B is the initial wavelength value under no strain state. The elastic-optic coefficient P_a is obtained by the calibration experiment.

4 Calibration experiment

The calibration experiment is divided into two parts: the measurement of material mechanical parameters and the calibration experiment of uniaxial compression. Firstly, the elastic modulus and Poisson's ratio of rock sample and epoxy resin sample are measured by uniaxial static load test. Then, the rock sample pasted with resistance strain gauge and FBG strain sensor is subjected to uniaxial compression. The FBG strain sensor is calibrated by measuring the strain with resistance strain gauge, and the elastic-optic coefficient of FBG sensor is calculated.

4.1 Construction of experimental platform

The experimental platform mainly includes rock true triaxial testing machine, resistance strain tester, FBG wavelength demodulator, granite cylinder sample and epoxy resin cylinder sample. FBG wavelength demodulator is used to measure the wavelength shift of FBG sensors, and its sampling frequency is set to 20Hz. Photos of the experimental platform are shown in Figure 8, and main parameters of the FBG wavelength demodulator are shown in Table 3.

(a) resistance strain tester   (b) FBG wavelength demodulator

| (c) rock true triaxial testing machine | (d) granite sample and epoxy resin sample |

Figure 8: The experimental platform.

Table 3: Main parameters of the FBG wavelength demodulator.

Parameter	Unit	Value
Wavelength measurement range	nm	1525-1565
Wavelength resolution	pm	1
Number of channels	\	4
Sampling frequency	Hz	1~2k
Minimum measurement interval	nm	0.5

220

In the experiment of mechanical parameters, three granite cylinders and one epoxy resin cylinder are selected as test samples. The center diameter of each sample is measured in three different directions, and the average value is taken as the effective value.

4.2 Determination of mechanical parameters of materials

225 The elastic modulus and Poisson's ratio were calculated by uniaxial compression test. Firstly, the UV glue was used to paste the resistance strain gauge at a specific position on the surface of the granite sample. 120Ω, 10 mm long resistance strain gauge is selected as the strain measurement unit. Four strain gauges are pasted on the surface of each specimen, two of which are in a group. Two strain gauges in each group were arranged along the axial direction and perpendicular to the axial direction, respectively. The longitudinal strain and transverse strain of the samples were measured during uniaxial 230 compression. The layout diagram and photos of strain gauge are shown in Figure 9(a).

(a)   (b)   (c)
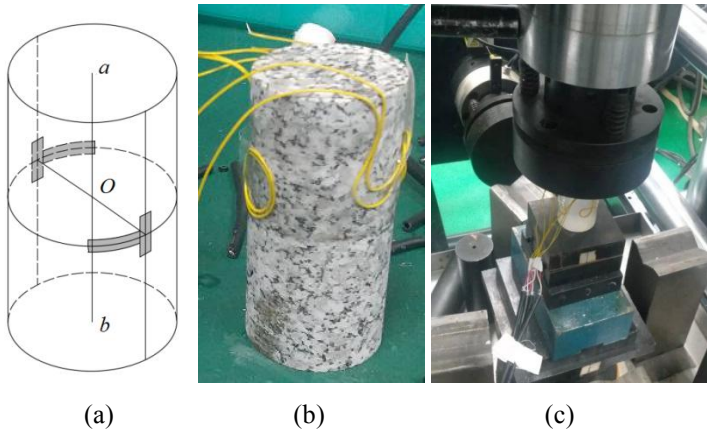
Figure 9: The layout diagram and photos of strain gauge.

235   Place the sample in the center of the z-axis hydraulic axis of the true triaxial testing machine, as shown in Figure 9(c). Then the axial load is applied to the sample, and the loading speed is set to be 1kN/s. when the axial force reaches 200kN, the loading stops (the loading speed of epoxy resin sample is 0.5kN/s, and the loading stops when the force reaches 100kN), and save the data file collected by strain gauge.

    The stress-strain curve was drawn by MATLAB 2012a software, and the mechanical parameters of materials were calculated.

240   Taking No. 1 granite sample as an example, Figure 10(a) shows the stress-strain curve, in which the red line l_h represents the relationship between stress σ and transverse strain ε_h, and the blue curve l_v represents the relationship between stress σ and longitudinal strain ε_v. The part of the two curves which is approximately a straight line (the red line segment and the blue line segment in Figure 10(b)) is intercepted, and the curve L v is fitted linearly (the black line segment in Figure 10(b)), and its slope is extracted as the elastic modulus E of the sample.

245

(a)   (b)
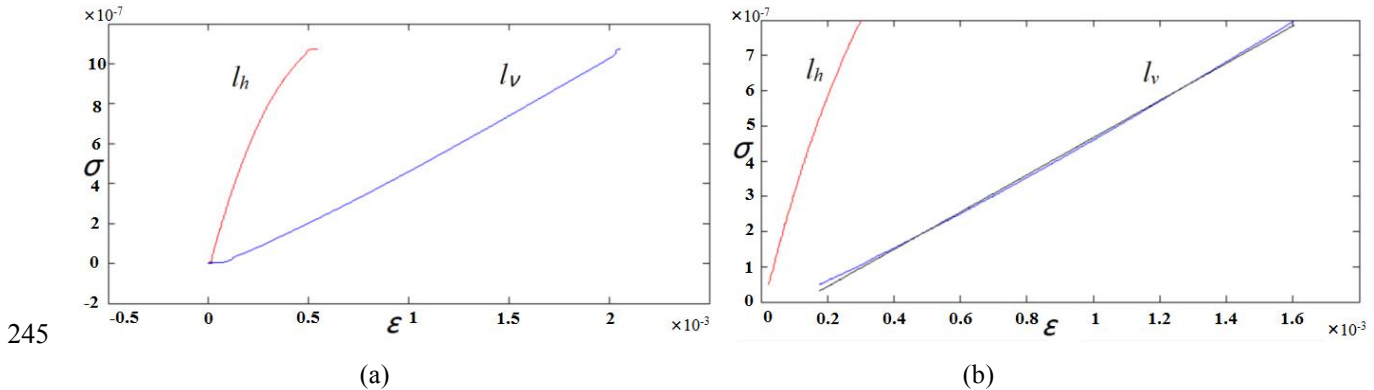
Figure 10: Calculation curve of mechanical parameters of materials.

As shown in Figure 11, the ratio of transverse strain ε_h to longitudinal strain ε_v is calculated, and its average value is taken as Poisson's ratio v of the sample.
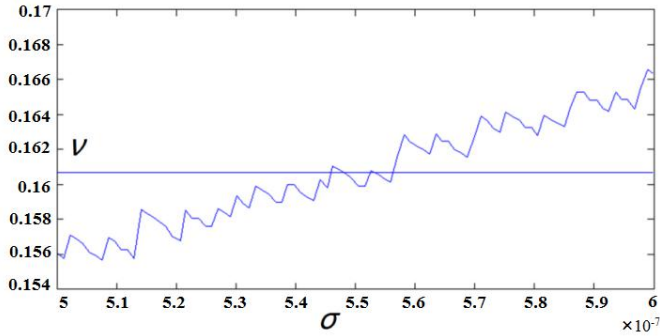
Figure 11: Calculation curve of Poisson's ratio.

Through several uniaxial compression tests, the arithmetic mean values of elastic modulus and Poisson's ratio of granite samples and epoxy resin samples are calculated, as shown in Table 3.

Table 3: Table of mechanical parameters of materials.

Samples parameters	Granite	Epoxy resin
E(GPa)	73.919	2.469
v	0.2518	0.4347

4.3 FBG sensor calibration

FBG sensor and resistance strain gauge are used to measure the longitudinal strain of cylindrical specimen under uniaxial compression, the strain measured by the resistance strain gauge is regarded as the actual strain of the sample, which is proportional to the wavelength shift ratio k_λ of the FBG. The linear correlation between them was analyzed and the elastic optical coefficient P_α was calculated.

As shown in Figure 12, two FBG sensors and two resistance strain gauges are pasted on the surface of granite samples. The pasting point is located on the circumference of the section perpendicular to the axis passing through the center point O of the cylinder, and the pasting direction is parallel to the axial direction. The two strain gauges are symmetrically distributed about the center of the axis, and the FBG pasting point is located at the interval of 90°. The symmetrical FBG can eliminate the influence of eccentric load.
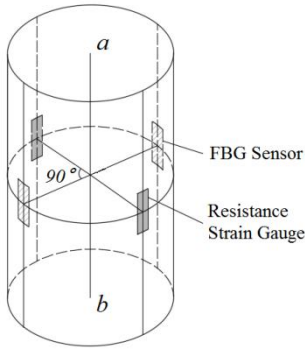
Figure 12: Schematic diagram of FBG sensor layout position.

270

The calibration test adopts multi-stage loading scheme, and the specific loading conditions are shown in Table 4.

Table 4: Calibration loading conditions of FBG sensor.

Condition	σ_1 (MPa)	Load(kN)	Speed(kN/s)
1	5.38	10	0.5
2	26.90	50	1
3	53.79	100	1

275   The average value $\overline{\varepsilon}$ of the two strain gauges is regarded as the actual value of the axial strain, and the average value k_λ of the wavelength shift ratio of the two FBG sensors is taken by the demodulator. After uniaxial loading, Matlab is used to process the test data, as shown in Figure 13.

(a)

(b)

(c)   (d)
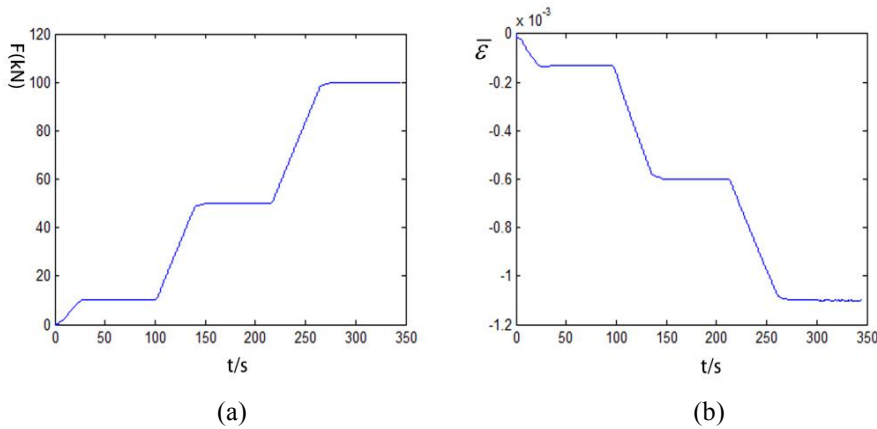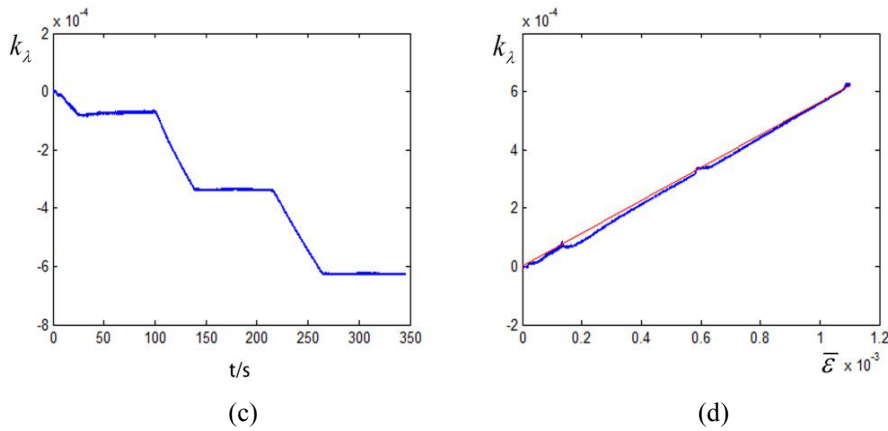
Figure 13: Schematic diagram of data processing in stress loading process.

280   Figure 13(a) shows the trend of axial load changing with time in the loading process, Figure 13(b) shows the relationship curve of strain variable of resistance strain gauge changing with time, and Figure 13(c) shows the relationship curve of FBG wavelength shift changing with time. These three parameters have obvious correlation. Figure 13(d) shows the relationship between strain of strain gauge $\overline{\varepsilon}$ and wavelength shift k_λ (blue curve). It shows that $\overline{\varepsilon}$ and k_λ have good linear relationship. When the strain range is less than 1000, the FBG strain sensor has good reliability.

285   The data group $\left(\overline{\varepsilon},\ k_\lambda\right)$ is fitted linearly, and then the slope of the red line in Figure 14 is taken as the linear relationship coefficient between wavelength drift and actual strain, and the elastic optical coefficient of FBG is calculated, and P_a =0.4369.

5 Finite element simulation of in-situ stress measurement

290   The ABAQUS finite element software is used to simulate the in-situ stress measurement process. According to the layout design, the linear strain in each FBG measurement direction is extracted. The stress is inversed by the stress inversion equation in Chapter 3, and compared with the applied load, which proves the theoretical validity and feasibility of the sensor assembly layout design and the stress inversion equation. It provides theoretical and data support for the trial production and application of the FBG hole-wall strain gauge.

295   The finite element numerical simulation process is divided into three stages: pre-processing, solution and post-processing. The pre-processing stage mainly includes model establishment, including meshing, defining material properties and assembling, determining interaction relationship and defining boundary conditions; The ABAQUS displacement method is used to solve the finite element problem in the solution stage. The relationship between force and displacement (unknown

quantity) is established and the stiffness matrix of the element is derived. The post-processing stage is mainly to display,
export and analyze the results based on the second step.

5.1 Establishment of calculation model

5.1.1 Model of each part

The CAE module of ABAQUS software is used to build the three-dimensional model of external rock mass, epoxy resin, hollow inclusion shell and piston guide, and the contact relationship between peripheral rock mass, epoxy resin and strain gauge is considered. The 3D model of each part is shown in Figure 14.

(a) External rock mass   (b) epoxy resin

(c) piston guide
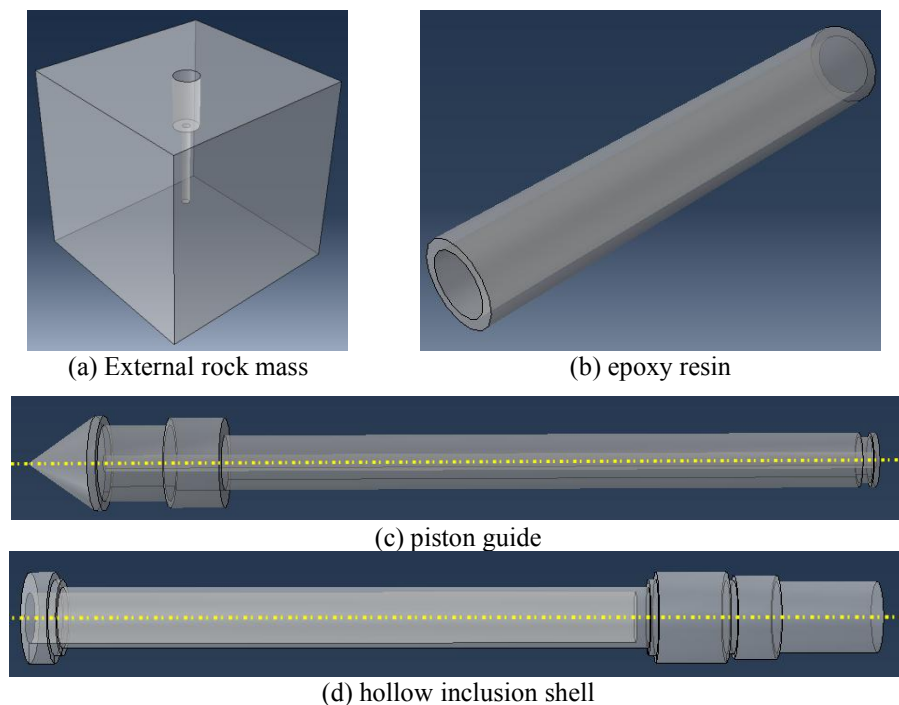
(d) hollow inclusion shell
Figure 14: The 3D model of each part.

5.1.2 Definition of material properties

In the stress measurement of overcoring method, rock mass and hollow inclusion are usually in elastic deformation stage (Cai, 2000). Therefore, the above four parts are defined as isotropic and homogeneous linear materials in the simulation. The mechanical parameters of granite and epoxy resin measured in uniaxial compression test (Section 4.2) are adopted. The specific mechanical parameters of each component are shown in Table 5.

Table 5: Calibration loading conditions of FBG sensor.

Parts	E(GPa)	v

Rock mass	73.191	0.2518
Epoxy resin	2.469	0.4347
Hollow inclusion shell	2.56	0.4
Piston guide	2.56	0.4

315

5.1.3 Defining contact surface and meshing

The four parts are assembled, as shown in Figure 15. There are three kinds of contact between the components: the contact between the epoxy resin and the hole-wall (contact 2), the contact between the epoxy resin layer and the hollow inclusion shell (contact 1), and the contact between the inner wall of the hollow inclusion shell and the piston guide part (contact 3). In

320   the simulation, tie constraint is applied on the outer wall of epoxy resin layer and the hole-wall to bind the contact nodes on the two surfaces, so that the contact nodes will not produce relative displacement and play the role of transferring the deformation of the hole-wall.
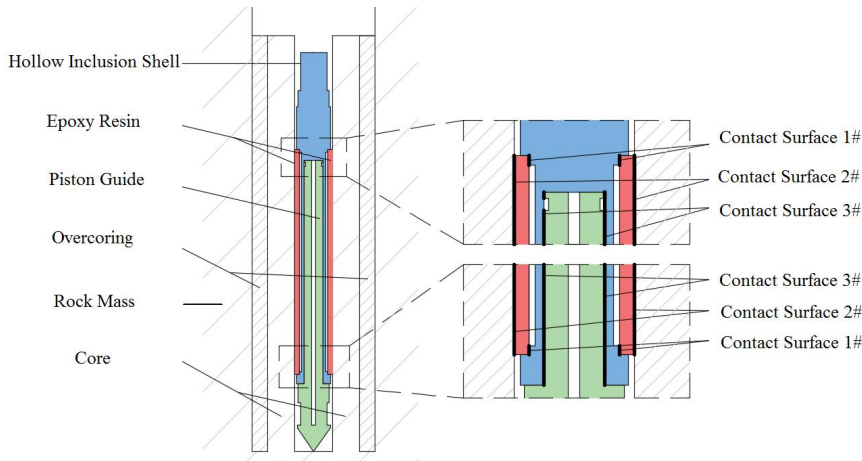
Figure 15: Assembly and contact surface setting diagram of each parts.

325

When meshing the epoxy resin layer, in order to guide the software to establish reference points at the nodes generated by FBG position, there should be intersection FBG position nodes at the points of FBG arrangement on the inner side of epoxy resin. As shown in Figure 16, the epoxy resin layer, as a direct part of strain measurement, increases the mesh density of the stressed part in order to improve the simulation accuracy.

330
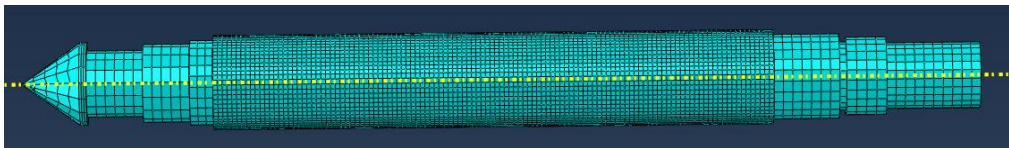
Figure 16: Meshing of the main structure and epoxy resin layer.

5.2 Result analysis

Because FBG sensor group is arranged between the hollow inclusion shell and the epoxy resin layer, the strain effect of the
335 core part and the epoxy resin layer before and after casing is analyzed and compared. Figure 17 shows the absolute
maximum principal strain nephogram of the core and epoxy resin before overcoring. The stress distribution of the two parts
is similar, and there is no obvious change in the vertical strain of the two components, and the boundary effect is not obvious.
It can be seen from the strain distribution in Figure 18 that the deformation coupling between the epoxy resin layer and the
hole-wall is satisfactory, and the epoxy resin layer can better transfer the deformation of the hole-wall under the simulated
340 in-situ stress.
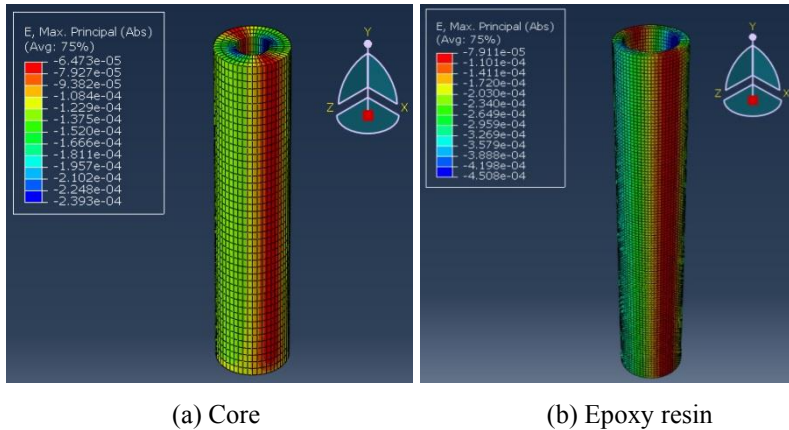
(a) Core   (b) Epoxy resin

Figure 17: The absolute maximum principal strain nephogram of the core and epoxy resin before overcoring.

345
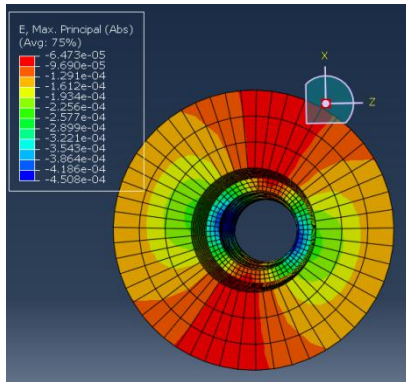
Figure 18: The deformation coupling between the epoxy resin layer and the hole-wall.

As shown in Figure 19, the strain in most areas of the core and epoxy resin disappears after the overcoring. The stress in the
strain measurement section is relieved successfully, and there is a large strain at the connection between the lower end of the
350 core and the rock mass.
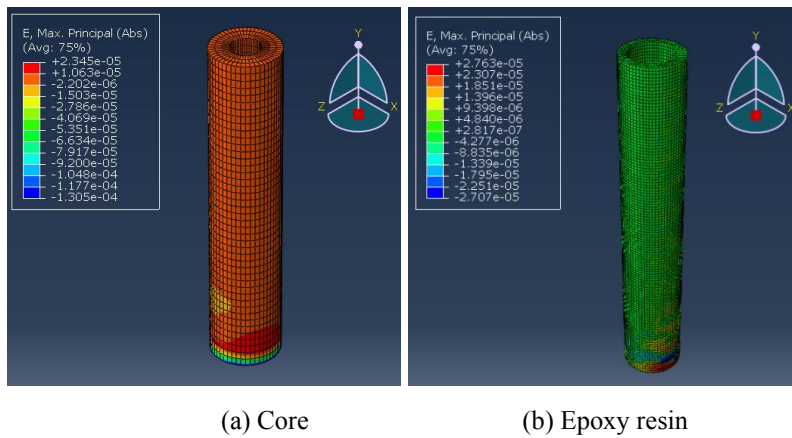
(a) Core   (b) Epoxy resin

Figure 19: The absolute maximum principal strain nephogram of the core and epoxy resin after overcoring.

355   As shown in Figure 20, there is a fixed interval and small strain fringe area at the bottom of the outer wall of the epoxy resin. There is no large strain in the hole-wall area corresponding to the strain fringe of the epoxy resin layer, and the strain fringe is just located on the plane of the core grid node. It is determined that the strain fringe is caused by the different grid densities of the core grid and the epoxy resin layer, In the simulation, the strain fringes may partially affect the results of stress inversion.

360
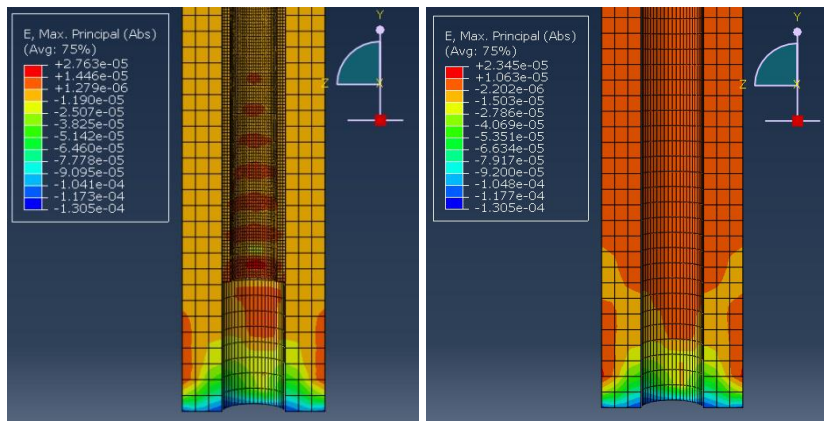
Figure 20: Strain nephogram in *y-z* direction of borehole and bottom area of epoxy resin layer.

5.3 Inversion of in-situ Stress

The linear strain of FBG in the measurement direction before and after the overcoring is extracted respectively, and the

365   difference (that is, the strain generated in the process of stress release) is brought into the in-situ stress inversion algorithm of

FBG sensor assembly to simulate the in-situ stress conditions, and the theoretical validity of the FBG sensor assembly design scheme is verified by comparing with the applied load.

5.3.1 Linear strain of the FBG sensor

According to the spatial symmetry of the sensor group, the twenty-six sensors are divided into seven equivalent orientations (see Section 2.2), the strain components before and after the overcoring are extracted respectively, and the stress inversion is carried out by taking the difference of the strain variables before and after the overcoring as the strain data. The simulated strain values of each FBG sensor are shown in Table 6.

Table 6: Strain value table of FBG sensors.

No.	Group	Azimuth	Axial angle(α=arctan0.75)	Strain value($\mu\varepsilon$)
1	a1	240°	α	93.280
2	a1	60°	-α	94.429
3	a1	240°	α	95.932
4	a1	60°	-α	92.379
5	a1	240°	α	94.858
6	a1	60°	-α	95.370
7	a2	0°	α	42.428
8	a2	180°	-α	41.248
9	a2	0°	α	45.150
10	a2	180°	-α	41.208
11	a2	0°	α	42.512
12	a2	180°	-α	45.049
13	a3	120°	α	144.691
14	a3	300°	-α	144.811
15	a3	120°	α	146.942
16	a3	300°	-α	143.065
17	a3	120°	α	146.123
18	a3	300°	-α	145.062
19	b1	225°	-45°	92.466
20	b1	45°	45°	94.902
21	b2	135°	45°	175.564

22	b2	315°	-45°	177.069
23	b3	45°	-45°	92.1093
24	b3	225°	45°	94.6346
25	b4	315°	45°	174.122
26	b4	135°	-45°	177.062

5.3.2 Calculation of in-situ stress inversion

Since the simulated working condition is vertical hole and does not involve coordinate system transformation, the values of parameters in Table 7 and the measured values of strain in Table 8 are substituted into the stress inversion equation (equation 8 in Section 3.2), and MATLAB 2012a is used for stress inversion analysis. Table 8 shows some intermediate variables in stress inversion calculation, and the results of in-situ stress inversion calculation are shown in Table 9.

Table 7: Stress inversion parameter table and correction factors of epoxy resin.

Symbol	Unit	Value	Definition
E	GPa	73.191	Elastic modulus of rock mass
G	GPa	29.234	Shear modulus of rock mass
v	-	0.2518	Poisson's ratio of rock mass
E'	GPa	2.469	Elastic modulus of epoxy resin
G'	GPa	0.8605	Shear modulus of epoxy resin
v'	-	0.4347	Poisson's ratio of epoxy resin
r	mm	20	Outer radius of epoxy resin
r'	mm	15	Inner radius of epoxy resin
ρ	mm	15	Radial distance of FBG in hollow inclusion
β_0	°	0	The angle between the x-axis of geodetic coordinate system and due north direction
K1		1.5179	
K2	-	1.4688	Correction factors of epoxy resin
K3		1.2624	
K4		1.6535	

Table 8: intermediate variables in stress inversion calculation.

	Symbol	Value	Symbol	Value
Intermediate variables	N1	0.3853	N2	-0.4952

of stress-strain matrix	N3	0.4901	N4	-1.7156
	N5	1.5171	N6	2.6276
	N7	0.6330	N8	0.2918
	N9	-2.7514	N10	2.2348

385

Table 9: Stress inversion results.

Symbol	Definition	Value	Symbol	Definition	Value
σ_x		9.0196	σ_1		9.3145
σ_y		5.2391	σ_2	Principal stress(MPa)	4.9442
σ_z	Stress component (MPa)	2.8639	σ_3		2.8639
τ_{xy}		1.0962	$\sigma_{h\max}$	Maximum horizontal stress(MPa)	9.3144
τ_{yz}		0.0034	$\sigma_{h\min}$	Minimum horizontal stress(MPa)	4.9442
τ_{xz}		0.0089	γ	The angle between the maximum horizontal stress and the counter clockwise X-axis	-16.1698°
SS_{res}	Residual Sum of Squares		4.4915×10^{-11}		

It can be seen from table 8 that the FBG sensor assembly is used to simulate strain measurement and inversion of in-situ stress. Compared with the applied stress as the actual value of in-situ stress, the measurement errors of three principal

390 stresses σ_1,σ_2,σ_3 and maximum horizontal stress angle γ are less than 10%, which are 6.86%, 1.12%, 4.54% and 7.80% respectively.

6 Data processing method

In the actual measurement of in-situ stress based on hollow inclusion method, there are often a few sensors with large errors, so it is judged as the abnormal value of strain. The traditional resistance strain gauge hole-wall measuring instrument

395 generally only has twelve strain sensors with six different equivalent measuring directions. The traditional hole-wall strain gauge based on resistance strain generally only has twelve strain sensors with six different equivalent measuring directions, so the abnormal values can not be easily removed in the process of solving the in-situ stress. The least square method is very sensitive to outliers, and the existence of outliers will have a great impact on the solution results, resulting in large errors in inversion stress.

400 The FBG strain sensor module designed in this paper distributes twenty-six sensors in seven equivalent positions, in which each equivalent position corresponds to six sensors, and each equivalent position of group B corresponds to two strain values.

Twenty-six strain data can be obtained in theory, so the fault tolerance rate of data and the reliability of stress inversion results are greatly improved. However, if we want to make full use of a large number of strain data, give full play to the advantages of large amount of quasi distributed measurement data, and get more real and reliable stress inversion results, we

405   still need to study reasonable data processing methods.

In this section, the box-plot method is used to eliminate the measurement data with abnormal residual absolute value in the least square solution. After two times of elimination operation, the overall reliability of the data can be effectively improved, and then the stress data such as the stress tensor, the size and direction of the principal stress and the maximum horizontal stress can be calculated. In order to meet the necessary conditions for solving the stress inversion equation (Equation 8), it is

410   necessary to judge whether the following two elimination conditions are satisfied: first, the abnormal strain values are eliminated in the order of absolute residual value from large to small; The second is to keep at least one strain measurement data in different equivalent measurement directions.

Taking the strain measurement data of numerical simulation in Chapter 5 as an example, SS_{res} is the sum of squares of strain residuals, which is used to measure the fitting degree of the stress data in the stress-strain equation obtained by the least

415   square method in the calculation. The larger SS_{res}, the lower the fitting degree of the least square solution. SS_{res} is calculated as follows:

$$SS_{res} = \sum_{i=1}^{n} r_i^2 \tag{15}$$

Where n is the number of strain variables and r_i is the residual error of the i-th strain. Figure 21(a) shows the distribution of the absolute value of the residual error of the original strain data. The ordinate represents the label of the FBG corresponding

420   to the residual error, the abscissa is the label of the corresponding FBG, and the absolute value of the residual error is small (less than2.5×10^{-6}), and which is evenly distributed. There is no abnormal value in the box-plot diagram (Figure 21 (b)), and the sum of squared residuals SS_{res} is very small, only in the order of 10^{-11}, which proves that the stress inversion results are ideal and reliable.

(a)
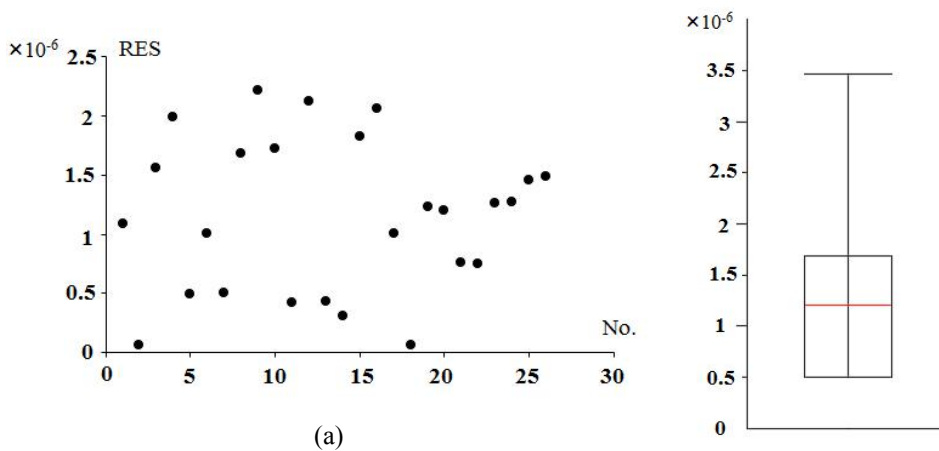
Figure 21: Residual error analysis of FBG strain measured data.

425

7 Conclusion

Combining the traditional in-situ stress measurement method with FBG sensing technology, this paper designs a FBG strain sensor group with the function of three-dimensional in-situ stress measurement, and then provides a direct and accurate observation method for the measurement of hole-wall strain by developing FBG strain sensor group, which can make up for

430 the shortcomings of the existing hole-wall strain gauge based on resistance strain gauge, which is of great theoretical and practical value for the development of in-situ stress measurement technology.

The highlights of this paper are as follows:

(1) Based on the layout of FBG strain sensor group, a new in-situ stress inversion algorithm is derived. The twenty-six FBG strain sensors connected in series with six optical fibers are divided into seven groups of equivalent measurement position,

435 the strain sensor group is installed by using the double area quasi-distributed winding method; the correction coefficients of epoxy resin are added to optimize the inversion equation of hole-wall strain and in-situ stress, to reduce the influence of the coupling effect of the hole-wall on the stress inversion results.

(2) The process of in-situ stress measurement has been simulated to verify measurement feasibility and data reliability of the FBG strain sensor group.Compared with the applied stress as the actual value of in-situ stress, the measurement errors of

440 three principal stresses σ_1, σ_2, σ_3 and maximum horizontal stress angle γ are less than 10%, which are 6.86%, 1.12%, 4.54% and 7.80% respectively. Through data processing method and error analysis, it is proved that FBG strain sensor array is feasible and reliable in the in-situ stress measurement based on overcoring method.

Data availability.

The data used to support the findings of this study are available from the corresponding author upon request.

445

Author contributions.

All authors contributed to this article, with the order of the authors' names reflecting the size of their contribution. YL, ZH and HZ discussed and wrote the original draft preparation, YL and LY designed the structure, ZH, HZ and YL built the calculation model, PW and LY calculated and analyse data, PW and HZ drew figures.

450

Competing interests.

The authors declare that there is no conflict of interest.

Financial support.

455 This research has been supported by the National Natural Science Foundation of China (41804089), and China Postdoctoral Science Foundation (2019M650782).

References

Amadei B. and Stephansson O. 1997. Rock stress and its measurement[M]. London: Chapman and Hall.
460 Cai M. 2000. Principle and technology of in-situ stress measurement[M]. Beijing: Science press. (in Chinese)
Cai M., Qiao L., Yu B., et al. 2000. Stress Measurement with an Improved Hollow Inclusion Technique In Jinchuan Nickel Mine[J]. International Journal of Minerals Metallurgy, 7(3):157-160. (in Chinese with English abstract)
Dewolf S., Wyatt F. K., Zumberge M. A., et al. 2015. Improved vertical optical fiber borehole strainmeter design for measuring Earth strain[J]. Review of entific Instruments, 86(11):1942-605.
465 Fama M., Pender M. J. 1980. Analysis of the hollow inclusion technique for measuring In Situ rock stress[J]. International Journal of Rock Mechanics & Mining Sciences & Geomechanics Abstracts, 17(3):137-146.

Feng W. Mechanics of materials (2nd Edition)[M]. Beijing:National defence industrial press, 2010.

Fuhr P. L., Spammer S. J., Jung C. C., et al. 1998. Fiber optic sensors in the Waterbury bridge[J]. SPIE, 3489:124-129.

Hill R. E., Peterson R. E., Warpinski N R, et al. 1993. Techniques for determining subsurface stress direction andassessing hydraulic fracture Azimuth[R]. SPE 29192,Eastern Regional Conference and Exhibition held in Charleston, WV, U.S.A.:8-10.

Hast, N. 1958. The measurement of rock pressure in mines, Årsbok[J]. Sveriges Geologiska Undersökning, Series C, 52, 1-183.

Hill K. O., Meltz G. 1997. Fiber Bragg grating technology fundamentals and overview[J]. Journal of Lightwave Technology, 15(8):1263-1276.

Hou Z. 2020. Research on quasi distributed three dimensiona hole-wall strain gauge based on Fiber Bragg grating[D]. Beijng: China University of Geosciences (Beijing). (in Chinese with English abstract)

Iabichino G., Isaia M., M Barbero. 2014. Development of a software for the interpretation of data obtained by CSIRO cell[J]. Geoingegneria Ambientale E Mineraria, 142(2):55-59.

Leeman E. R. 1964. The measurement of stress in rock: Part II: Borehole rock stress measuring instruments [J]. Journal of the Southern African Institute of Mining and Metallurgy, 65(2):254-284.

Leeman E. R. 1971. The CSIR Doorstopper and triaxial rock stress measuring instrument[J]. Rock Mechanics, 3(1):25-50.

Liu Y., Yin J., Liu Y. 2011. Measuring techniques for hollow inclusion triaxial strain cells[J]. Chinese Journal of Geotechnical Engineering, 33(2):291-296. (in Chinese with English abstract)

Maccioni E., Giacomelli U., Carbone D., et al. 2019. Shallow bore-hole three-axial fiber Bragg grating strain sensor for Etna volcano monitoring[J]. Review of Scientific Instruments, 90(9):094501.

Ou J. 2005. Reseach and practice of smart sensor networks and health monitoring systems for civil infrastructures in mainland China[J]. Bulletin of National Natural Science Foundation of China, 19(1):8-12. (in Chinese with English abstract)

SJÖBERG J., KLASSON H. 2003. Stress measurements in deep boreholesusing the Borre(SSPB) probe[J]. International Journal of Rock Mechanics and Mining Sciences and Geomechanics Abstracts, 40(7):1205-1223.

Wang C. 2014. Brief Review and Outlook of Main Estimate and Measurement Methods for in-situ Stresses in Rock Mass[J]. Geological Review, 60(5):971-996. (in Chinese with English abstract)

Ulusay R. 2014. The ISRM Suggested Methods for Rock Characterization, Testing and Monitoring: 2007-2014[J]. Springer International Publishing, 15(1):47-48.

Worotnicki, G. and Walton, R. 1979. Virgin rock stress measurements at the Warrego Mine[R]. CSIRO Tech. Rept. No. 93, Melboune.

Yan Z., Guo Q., Wang P. 2018. Calculation and application of in-situ stress components in hollow inclusion measurement[J]. Rock and soil mechnical, 39(2):715-721. (in Chinese with English abstract)

Zhang W., Liang L., Zhao Q., et al. 2001. Contract analyses of strain measurement of fiber grating and resistance strain chip[J]. Journal of Transduction Technology, 14(3):200-205. (in Chinese with English abstract)

Zhong Z., Chen Y., Luo C., et al. 2002. Technique of geostress measurement in deep borehole by hellow inclusion triaxial strain gauge[C]. Chinese Rock Mechanics and Engineering Institute Seventh Academic Conference Proceedings:713-715. (in Chinese with English abstract)

Zhong Z., Zhao B., Lin J. et al. 2018. Three dimensional in-situ stress sensor based on optical fiber sensing technology[J]. Optical and precision engineering, 26(2):325-335. (in Chinese with English abstract)

Zhou C., Chen W., Liu Y., et al. 2010. Study on GI-I multi-parameter fiber monitoring system for geological disasters[J]. Exploration Engineering(Rock & Soil Drilling and Tunneling), 37(1):31-34. (in Chinese with English abstract)